Motion of Buoyant, Flexible Aquatic Vegetation Under Waves: Simple Theoretical Models and Parameterization of Wave Dissipation

Henderson, Stephen M.[a,*]

[a]*School of the Environment, Washington State University (Vancouver). Vancouver, WA 98686, USA*

Abstract

When submerged, flexible vegetation bends back and forth under waves, and stems are tilted only a small angle from vertical, simple models for stem motion and wave dissipation can be derived. Here, previous simple models for the wave-induced bending of elastic vegetation are extended to account for buoyancy. Buoyancy results in stem tension which, together with fluid drag, is incorporated in the Euler-Bernoulli problem, in which each stem is modeled as a cantilevered elastic beam. Solutions are governed by a new 'dimensionless buoyancy' β, in addition to the 'dimensionless stiffness' S identified by previous researchers. If $\beta \ll S^{1/2}$, buoyancy is negligible and previous results for elastic stems are recovered. Specifically, stems are nearly immobile for $S \gg 1$, but for $S \ll 1$ stems move with surrounding water except in a thin 'elastic boundary layer' extending a distance $S^{1/4}l_*$ above the bed, where $l_* =$ stem length. Conversely, if $\beta \gg S^{1/2}$, then elasticity is negligible along most of the length of the stem and new behaviour is found. Specifically, stems are nearly immobile for $\beta \gg 1$, but for $\beta \ll 1$ stems move with surrounding water except in a thin 'buoyant boundary layer' extending a distance $\beta^{1/2}l_*$ above the bed. For essentially inflexible cases ($S \gg 1$ or $\beta \gg 1$), simulated depth-integrated wave dissipation roughly equals the value D_r predicted for rigid stems. For highly flexible cases (i.e. for S and β both $\ll 1$), dissipation is limited to elastic or buoyant boundary layers, and therefore scales with the maximum of $S^{1/4}D_r$ and $\beta^{1/2}D_r$. For the simple stems considered here, which have constant diameter and density, simulated dissipation for all S and β was approximated by the expression $[(S+\beta^2/4)/(4+S+\beta^2/4)]^{1/4}D_r$. This simple formula may require

*corresponding author email: steve_henderson@wsu.edu; ph: USA (503) 706 8819

modification for vegetation with complex geometry. Nevertheless, this analysis identifies β as a key parameter for inclusion in dissipation formulations, together with parameters such as S identified by previous authors.

Keywords:
Flexible vegetation, Wave dissipation, Oscillatory flows, Kelp, Seagrass, Fluid-solid interaction

---

Highlights

- Dissipation is predicted for waves propagating through flexible vegetation.
- Force-balance model analyzed for small-tilt motion of buoyant, elastic stems.
- New dimensionless buoyancy quantifies buoyant resistance to oscillatory motion.
- A simple expression approximates depth-integrated wave dissipation.
- Results may aid assessment of coastal protection by wetlands.

1. Introduction

Flexible vegetation canopies are widespread in lakes, estuaries, and coastal oceans. Examples include saltmarshes, kelp forests, and seagrass meadows. Aquatic vegetation provides numerous ecological and economic benefits (Brander et al., 2006; Greenberg et al., 2006; Gren, 1995; Siikamäki et al., 2012). In a world of rising sea levels, the ability of aquatic vegetation to provide coastal protection, by sheltering coastlines from energetic waves, has drawn particular attention (Arkema et al., 2013; Broekx et al., 2011; Feagin et al., 2015; Jones et al., 2012; Möller et al., 2014; Temmerman et al., 2013). Here, a model is developed to quantify the dissipation of waves by flexible vegetation.

Wave dissipation can be intense in some vegetation canopies (Jadhav et al., 2013; Riffe et al., 2011), but can be greatly reduced if stems are sufficiently flexible to move with the surrounding water (Elwany et al., 1995; Koehl, 1984; Rosman et al., 2007; **?**). Consequently, models for dissipation by rigid vegetation (Dalrymple et al., 1984; Henderson et al., 2017; Lowe et al., 2005) must be modified when vegetation is flexible. Empirical models have been developed by fitting measured dissipation in flexible canopies to functions of the Reynolds number $R_e = u_{0*} r_* / \nu_*$ and the Keulegan-Carpenter number $K_c = u_{0*} t_{0*} / (2 r_*)$, where u_{0*} = amplitude of velocity fluctuations near the seabed, r_* = stem radius, ν_* = kinematic viscosity, and t_{0*} = wave period (Augustin et al., 2009; Blackmar et al., 2014; Bradley and Houser, 2009; Jadhav et al., 2013; Kobayashi et al., 1993; Mendez and Losada, 2004). Resulting empirical formulas yield good results when tuned for a specific

species and growth stage, but do not explicitly account for many of the parameters influencing stem motion, including stem length, Young's Modulus, and buoyancy. These unaccounted-for parameters differ between plants by orders of magnitude (e.g. for stem lengths compare Utter and Denny (1996) with Bradley and Houser (2009), and for Young's modulus compare Utter and Denny (1996) with Zhang et al. (2015)) or sign (e.g. for buoyancy see Stewart (2006)). Consequently, differing R_e- and K_c-based formulations are required for differing species (Mullarney and Henderson, 2018).

As an alternative to empirical parameterization, models can be developed from an understanding of coupled fluid-solid mechanics. For steady currents, extensive research has identified key parameters quantifying the balance between the forces of fluid drag, elasticity, and buoyancy. The dimensionless Cauchy number C_a controls stem bending when elastic and drag forces balance, with minimal bending when $C_a \ll 1$, and order-one stem tilt when $C_a = 1$ (for definitions of C_a and other variables, see table 1). For $C_a \gg 1$, bending is concentrated along a small near-bed section of the stem, with the remainder of the stem almost aligned with the flow. A dimensionless buoyancy parameter, denoted P by Nikora et al. (1998), controls bending when buoyant and drag forces balance, with minimal bending when $P \ll 1$ (the relative importance of buoyancy and elasticity is controlled by the parameter $B \sim C_a/P$, Luhar and Nepf, 2011, where '$\sim$' indicates equality except for an order-one constant).

For oscillatory flows under waves, comprehensive numerical models have been developed to simulate stem motion (Luhar and Nepf, 2016; Utter and Denny, 1996; Zeller et al., 2014). When stem tilts are small, equations for drag and stem bending can be approximately linearized and analytic solutions can be obtained. Mullarney and Henderson (2010) (hereafter MH10) found analytic solutions for the case of negligible stem buoyancy. Here, the MH10 model is extended to account for buoyancy.

The model of MH10 highlights the importance of a 'dimensionless stiffness' S. This stiffness quantifies the competing effects of elastic stresses, which resist stem bending, and fluid drag, which acts to bend stems. For $S \gg 1$ stems are nearly rigid, whereas for $S \ll 1$ stems mostly move back and forth with surrounding water. However, attachment to the bed limits the near-bed motion of even the most flexible stems. Consequently, for $S \ll 1$, theory predicts an 'elastic boundary layer', extending a distance $S^{1/4} l_*$ above the bed, within which elastic forces cause substantial differences between water and stem motions [this elastic boundary layer, where elastic

forces acting on stems are substantial, differs from the familiar wave bottom boundary layer (hereafter WBBL), where shear stresses acting on the water are substantial]. Since wave dissipation requires relative motion between stems and surrounding water, simulated dissipation in highly flexible vegetation is limited to the elastic boundary layer, and depth-integrated dissipation is reduced from the rigid value by a factor of order $S^{1/4}$ [hereafter denoted $O(S^{1/4})$]. In laboratory experiments, Luhar et al. (2017); Luhar and Nepf (2016) found that dissipation in canopies of flexible artificial vegetation was consistent with this scaling over a wide range of S, even for moderate stem tilts. In field experiments, Riffe et al. (2011) found that bulk wave dissipation within a natural canopy of moderately flexible sedge was also consistent with MH10 theory.

Luhar and Nepf (2016) presented an insightful explanation for the relationship between the Cauchy number C_a, governing elastic bending under steady flows, and the dimensionless stiffness S, governing oscillatory flows. For steady flows, leading-order drag reduction occurs as stems are bent flat, which requires horizontally displacing the stem tip a distance comparable to the stem length l_*, with transition to this behaviour occurring as C_a becomes greater than 1 (Figure 1a). In contrast, for oscillatory flows, stems need not bend flat for major drag reduction to occur (Figure 1b). Instead, drag reduction in oscillatory flows can occur when the stem is displaced a distance comparable to the 'orbital displacement scale' W_{0*}, with such bending occurring when S is less than about 1 (neglecting a factor of π, discussed below, W_{0*} is the distance water particles move back-and-forth under waves). Therefore, when $W_{0*} \ll l_*$, much less bending is required for leading-order drag reduction under waves than under currents. In terms of the 'dimensionless stem length' $L = l_*/W_{0*}$, this result can be restated in a more quantitative manner: When $L \gg 1$, leading-order drag reduction requires order L^{-1} less stem displacement under waves than under steady currents. Since elastic forces are roughly proportional to stem displacement, this suggests $S \sim (C_a L)^{-1}$, as was confirmed by Luhar and Nepf (2016).

The scaling arguments of Luhar and Nepf (2016) neglected buoyancy. However, we note that adapting their reasoning for buoyancy-dominated cases suggests that bending is controlled by a 'dimensionless buoyancy' $\beta \sim (PL)^{-1}$. For oscillating flows with negligible elastic stiffness, detailed analysis below confirms that stem bending is indeed controlled by β. Specifically, stems move much less than surrounding water particles when $\beta \gg 1$, whereas stems move with surrounding water except in a near-bed 'buoyant boundary

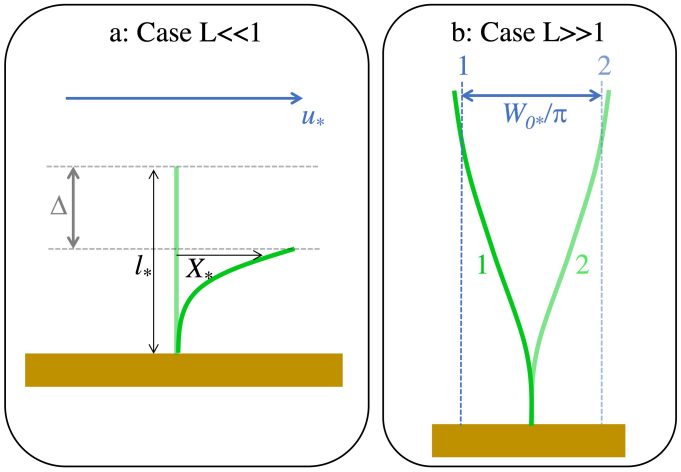

Figure 1: Drag reduction mechanisms in flexible vegetation. For small dimensionless length [panel a, $L \ll 1$, where $L = (\text{stem length})/(\text{water particle displacement})$], drag reduction occurs when an initially vertical stem (light green line) is bent (dark green curve) by water velocity u_*, so that water over a range of elevations (labeled Δ) does not experience vegetation drag. For this mechanism to yield leading-order drag reduction, stem tilts must be order-one, so the horizontal stem displacement X_* must be comparable to the stem length l_*. For large dimensionless length (panel b, $L \gg 1$), a different drag reduction mechanism operates. Specifically, as water particles are displaced alternately left (vertical dashed blue line labeled 1) and right (dashed blue line 2), a sufficiently flexible stem is displaced alternately left (dark green curve 1) and right (light green curve 2), so that the upper portion of the stem moves with surrounding water. Drag on the stem's upper section is then reduced, because water motion relative to the stem is reduced. For this mechanism to yield leading-order drag reduction, the horizontal stem displacement X_* must be comparable to the water particle displacement (i.e. order-W_{0*}), so stem tilt must be order $W_{0*}/l_* = L^{-1} \ll 1$. This small tilt required for drag reduction when $L \gg 1$ (panel b) contrasts with the order-one tilt required for drag reduction when $L \ll 1$ (panel a), accounting for an order-L difference between dimensionless parameters governing drag reduction in the two cases. Note that the drag-reduction mechanism of panel b cannot apply when $L \ll 1$, because stems are then too short to move with the surrounding water. Furthermore, the mechanism of panel a cannot apply when $L \gg 1$, because water particles then do not move sufficiently to generate order-one tilt.

layer' when $\beta \ll 1$.

This paper presents models for bending along the length of a continuous stem, neglecting stem inertia. This approach contrasts with some previous models for buoyant vegetation, which represented inertia, drag and buoyancy as if they acted at a single point, attached to the seabed by a thin, straight, non-buoyant rope (Denny and Gaylord, 2002; Denny et al., 1997; Stevens et al., 2001; Utter and Denny, 1996). When inertia is neglected, we show that vegetation motion in these previous 'buoy on rope' models is also governed by β. However, such models do not resolve motion along the length of a continuous stem, and do not resolve the buoyant stem boundary layer.

We start by simplifying and non-dimensionalizing equations previously used for numerical modeling of elastic, buoyant stems (Luhar and Nepf, 2016) for the case of small stem tilts (Section 2). Resulting scaling parameters are compared with parameters governing previous steady-flow and buoy-on-rope models (Section 3). Solutions are presented for depth-uniform flows (Section 4), considering in turn nonlinear numerical simulations (Section 4.1) and linearized analytic solutions (Section 4.2). For small S and β, boundary layer solutions reveal that the buoyant boundary layer thickness scales with $\beta^{1/2} l_*$ (Section 5). To facilitate the development of models for practical applications, we show that depth-integrated wave dissipation is well approximated by a straightforward function of S and β in the case of simple stem geometries (Section 6). Applications and limitations of analysis are illustrated by considering a range of natural vegetation (Section 7) and results are summarized (Section 8).

2. Model equations and scaling

Four forces acting on stems will be considered:

1. The elastic shear force V_* (i.e. the elastic shear stress integrated over the stem's cross-sectional area), which resists stem bending. From Euler-Bernoulli theory for the bending of thin beams (e.g. Luhar and Nepf, 2016; Niklas, 1992), $V_* = -\partial/\partial s_*(E_* I_* \partial\theta/\partial s_*)$, where $s_* =$ along-stem distance measured from stem base, $\theta =$ stem tilt from vertical (in radians), $E_* =$ Young's modulus, and the second moment of stem area $I_* = \int \chi_*^2 \, dA_*$, where $\chi_* =$ distance in flow direction from center of stem, and the integral is taken over the stem's cross-section (for circular cross-section, $I_* = \pi r_*^4/4$, where $r_* =$ stem radius, Niklas, 1992). Throughout, stars indicate dimensional variables.

2. The upward buoyant force per unit length of stem

$$f_{b*} = \rho_* b_* A_*, \tag{1}$$

where the stem buoyancy $b_* = g_*(\rho_* - \rho_{s*})/\rho_*$, $g_* = 9.8\,\mathrm{ms}^{-2}$, $\rho_* =$ water density, $\rho_{s*} =$ stem density, and $A_* =$ stem cross-sectional area.

3. The stem tension force T_* which, for small stem tilts, will balance stem buoyancy.

4. The drag force per unit length of stem f_{D*}. Stems that are susceptible to bending by waves often have diameters much less than the orbital displacement (e.g. for seagrasses, sedges, and kelp, stem diameters often range from $0.8-2\,\mathrm{cm}$, while in estuaries and the coastal ocean, orbital displacements often range from $10-200\,\mathrm{cm}$, Section 7). Therefore, we assume a large Keulegan-Carpenter number K_c. This large K_c suggests negligible acceleration-dependence of drag (Mullarney and Henderson, 2018; Sumer and Fredsøe, 1997; Zeller et al., 2015), leading to

$$f_{D*} = r_* \rho_* C_D \tilde{u}_* (u_* - u_{s*}) \tag{2}$$

where C_D is a drag coefficient, u_* and u_{s*} are time-dependent water and stem velocities, and in fully nonlinear drag formulations $\tilde{u}_* = |u_* - u_{s*}|$ where vertical bars ($|\cdot|$) denote absolute value. Analytic solutions will be obtained by linearizing this expression for drag following Borgman (1967); Henderson et al. (2017); Jadhav et al. (2013); Lowe et al. (2007); Mullarney and Henderson (2010). In this linearized formulation, we replace time-varying $\tilde{u}_*$ with a time-constant value. It will prove convenient to express this constant value in terms of a parameter ξ, which is defined such that

$$\tilde{u}_* = \frac{8}{3\pi} \xi u_{0*}. \tag{3}$$

This expression is chosen because, for sinusoidal velocity fluctuations and rigid stems ($u_{s*} = 0$), the mean squared error between linear and nonlinear drag parameterizations is minimized by setting $\xi = 1$. For mobile stems, the optimal ξ will be found by model tuning to be slightly less than 1 (likely because $|u_* - u_{s*}| < |u_*|$ when stem motions follow water motions).

Neglecting stem-parallel skin friction and terms of order K_c^{-1} (which include Froude-Krylov force, added mass, and stem inertia), the stem momentum equation (e.g. Luhar and Nepf, 2016, their equation 7) reduces to the

force balance

$$\frac{\partial}{\partial s_*}[(V_* + iT_*)e^{-i\theta}] + if_{b*} + f_{D*}e^{-i\theta} = 0, \tag{4}$$

where the real and imaginary components respectively represent horizontal and vertical forces.

For small stem tilt ($\theta \ll 1$), the along-stem derivative $\partial/\partial s_*$ can be approximated by the vertical derivative $\partial/\partial z_*$ (z_* measured upwards from the bed), with neglected error $O(\theta^2)$ [where $O(\theta^2)$ indicates a term of order θ^2]. Furthermore, elastic and drag forces are almost horizontal [vertical components $O(\theta)$], and can be neglected in the leading-order vertical component of (4). Integrating the imaginary component of (4) from any elevation z_* to the stem tip (where $T_* = 0$), neglecting contributions from vertical elastic and drag forces, and applying (1) then yields the leading-order vertical force balance

$$T_* = \rho_* b_* \mathcal{V}_*, \tag{5}$$

where $\mathcal{V}_* = \int_{z*}^{l_*} A_*\, dz_*$ is the stem volume above z_*. Therefore, at leading order, stem tension balances buoyancy. Taking the real part of (4), noting that $e^{-i\theta} = 1 - i\theta + O(\theta^2)$, and neglecting $O(\theta^2)$ terms, yields the leading-order horizontal force balance

$$-\frac{\partial^2(E_* I_* \partial\theta/\partial z_*)}{\partial z_*^2} + \frac{\partial(T_*\theta)}{\partial z_*} + f_{D*} = 0. \tag{6}$$

Although buoyancy does not directly exert a horizontal force, it is responsible for stem tension (5), which can exert a horizontal force when stems tilt [second term of (6)]. If elastic forces (first term) are negligible, (6) is a vertically inverted form of the classic oscillating, hanging chain problem (e.g. problem 24.4 of Simmons, 1972). If buoyant forces are negligible, (6) is the model of MH10.

To clarify the magnitude of terms in (5) – (6), introduce the dimensionless variables

$$z = z_*/l_*, \tag{7}$$

$$r = r_*/r_{0*}, \tag{8}$$

$$I = I_*/I_{0*}, \tag{9}$$

$$\mathcal{V} = \mathcal{V}_*/\mathcal{V}_{0*}. \tag{10}$$

where r_{0*}, I_{0*} and $\mathcal{V}_{0*}$ are typical magnitudes of r_*, I_* and $\mathcal{V}_*$. For simple stem geometries (e.g. nearly cylindrical stems), we choose to scale I_* and $\mathcal{V}_*$ with

$$I_{0*} = r_{0*}^4, \tag{11}$$
$$\mathcal{V}_{0*} = r_{0*}^2 l_*. \tag{12}$$

Let t_* be time, let X_* and W_* be horizontal stem and water displacements, and let corresponding dimensionless variables be

$$t = t_*/t_{0*}, \tag{13}$$
$$X = X_*/W_{0*}, \tag{14}$$
$$W = W_*/W_{0*}, \tag{15}$$

where

$$W_{0*} = u_{0*} t_{0*}. \tag{16}$$

For sinusoidal waves, W_{0*} defined by (16) is a factor of 2π greater than the amplitude of water particle displacements. Further define $u = u_*/u_{0*}$, $u_s = u_{s*}/u_{0*}$ and $\tilde{u} = \tilde{u}_*/u_{0*}$, so nonlinear and linear drag formulations respectively yield $\tilde{u} = |u - u_s|$ and $\tilde{u} = 8\xi/(3\pi)$. Assume simple stem geometry, so that (11) and (12) apply. Now noting that $\theta \approx \partial X_*/\partial z_*$ and combining (5) – (6) yields the governing equation for buoyant, elastic stem motion:

$$S\frac{\partial^2}{\partial z^2}\left(I\frac{\partial^2 X}{\partial z^2}\right) - \beta\frac{\partial}{\partial z}\left(\mathcal{V}\frac{\partial X}{\partial z}\right) = r\tilde{u}\frac{\partial(W - X)}{\partial t}, \tag{17}$$

where we have used $u - u_s = \partial(W - X)/\partial t$, the dimensionless stiffness (previously defined by MH10) is

$$S = \frac{E_* r_{0*}^3 t_{0*}}{\rho_* C_D l_*^4 u_{0*}}, \tag{18}$$

and the dimensionless buoyancy (not identified by previous researchers) is

$$\beta = \frac{b_* r_{0*} t_{0*}}{C_D l_* u_{0*}}. \tag{19}$$

For more complex stem geometries, S and β in (17) are replaced by

$$\tilde{S} = \frac{E_* I_{0*} t_{0*}}{\rho_* C_D l_*^4 r_{0*} u_{0*}}, \tag{20}$$

and

$$\tilde{\beta} = \frac{b_* \mathcal{V}_{0*} t_{0*}}{C_D l_*^2 r_{0*} u_{0*}}, \tag{21}$$

where we take r_{0*} as half the stem width in the direction normal to the flow. We will present results for cylindrical stems in terms of S and β, but for more complex geometries, $\tilde{S}$ and $\tilde{\beta}$ are preferred (Section 6).

Boundary conditions at the bed are

$$X|_{z=0} = 0, \tag{22}$$

$$\left.\frac{\partial X}{\partial z}\right|_{z=0} = 0. \tag{23}$$

Boundary conditions at the stem tip are

$$\left.\frac{\partial^2 X}{\partial z^2}\right|_{z=1} = 0, \tag{24}$$

$$\left.\frac{\partial^3 X}{\partial z^3}\right|_{z=1} = 0. \tag{25}$$

The model (17), (22) – (25) is equivalent to the model of MH10, except for the addition of buoyancy-induced tension [second term on the left of (17)].

By inspection of (17), for $S \gg 1$ or $\beta \gg 1$, elasticity or buoyancy is sufficient to prevent almost all stem motion ($X \ll 1$). Conversely, for $S \ll 1$ and $\beta \ll 1$, stems must move with the surrounding water along much of the stem length (so $|W - X| \ll 1$). Satisfaction of (22) by very flexible stems then requires a near-bed Stem Boundary Layer (SBL) where elasticity and/or buoyancy become significant.

3. Comparison with previous scaling parameters

The parameters S and β governing small-tilt oscillatory stem motion are related to parameters governing stem bending under steady flows (Section 1). Specifically, under steady flows, stem bending is controlled by the Cauchy number (de Langre, 2008)

$$C_a = \frac{\rho_* r_{0*} u_{0*}^2 l_*^3}{E_* I_{0*}}, \tag{26}$$

and the buoyancy parameter (Nikora et al., 1998)

$$P = \frac{C_D u_{0*}^2}{b_* r_{0*}}, \tag{27}$$

where we have rewritten the *Nikora et al.* expression in terms of near-bed velocity, and for simplicity omitted a factor of π. Comparing (18) – (19) with (26) – (27) (and neglecting the order-one factor C_D) yields $S = (C_a L)^{-1}$ and $\beta = (PL)^{-1}$, as anticipated in Section 1.

An additional dimensionless combination considered by Luhar and Nepf (2011) is $B \sim C_a/P$, which is roughly the ratio between buoyant and elastic forces for bending under steady flows. The dimensionless buoyancy β is related to B by $\beta \sim BS \sim B(CaL)^{-1}$. Therefore, only three of the six dimensionless variables S, β, L, Ca, P and B are independent.

Having defined the governing dimensionless parameters, we summarize the relationship between previous research and the work presented here as follows: For steady flows $W_{0*} \to \infty$, so $L = 0$. Therefore, a slowly-varying form of steady-flow analysis (de Langre, 2008; Luhar and Nepf, 2011) likely applies in the limit $L \ll 1$, as noted previously by Luhar and Nepf (2016). For $L \gg 1$, MH10 analyzed the case $\beta = 0$. The original contribution here is to analyze the $L \gg 1$ case for non-zero β. Of the six dimensionless variables noted above, only S and β are considered below, because these yield the simplest expressions in oscillating flow cases with $L \gg 1$. However, if desired, results can be re-expressed in terms of other parameters such as C_a, P, and L, as was previously done for the elasticity-dominated case by Luhar and Nepf (2016).

The parameter β also plays a key role in previous buoy-on-rope models for buoyant vegetation (e.g. Denny et al., 1997; Utter and Denny, 1996). Under the large-K_c approximation discussed above and neglecting vertical water motion, equation 15 of Utter and Denny (1996) reduces to the force balance

$$iT_* e^{-i\theta} + iF_{b*} + F_{D*} = 0, \tag{28}$$

where real and imaginary parts represent horizontal and vertical forces, and buoyant and drag forces integrated along the length of the stem (F_{b*} and F_{D*}) are treated as if they acted at a single point. From the small-tilt vertical force balance $T_* \approx F_{b*}$. The leading order horizontal force balance is then

$$\tilde{\beta} X = \tilde{u} \frac{\partial (W - X)}{\partial t}, \tag{29}$$

as can be established by noting $F_{b*} = \rho_* b_* \mathcal{V}_{0*}$, $F_{D*} = l_* r_* \rho_* C_D \tilde{u}_* \partial(W_* - X_*)/\partial t_*$ and $e^{-i\theta} \approx 1 - i\theta \approx 1 - iX_*/l_*$. By inspection, buoyancy prevents almost all stem motion when $\tilde{\beta} \gg 1$, whereas stems move with surrounding water ($|W - X| \ll 1$) when $\tilde{\beta} \ll 1$. Therefore, although previous buoy-on-rope models of buoyant vegetation accounted for additional physics not considered here (such as inertia, Denny et al., 1998), these previous models are governed by the parameter β when the approximations considered in this paper are applied.

4. Motion of Entire Stems in Depth-Uniform Flows

This section presents solutions for cases where the water velocity is nearly uniform along the length of the stem. This requires that stem length is much less than $(2\pi)^{-1}\times$wavelength, and that stem length is much greater than WBBL thickness. Water motion in fact depends on stem friction, potentially leading to complex depth-dependence of water velocity, but the density of many natural canopies is sufficiently low that this effect can be neglected (Dalrymple et al., 1984; Henderson et al., 2017; Lowe et al., 2005). Analytic solution for arbitrary depth-dependence is possible using normal mode expansions following MH10, but for simplicity is omitted here.

4.1. Nonlinear drag

Finite difference solutions to (17), (22) – (25) were obtained for sinusoidal water velocity $u = \cos(\omega t)$, with $\omega = 2\pi$ (corresponding to dimensionless period 1 and dimensional period t_{0*}). A uniformly spaced numerical grid was used, with 150 time steps per period, and either 100, 200, or 400 vertical gridpoints (the higher resolutions were used for SBL cases). For each time step, following the Crank-Nicholson approach (Morton and Mayers, 2005), elastic and buoyant terms [left of (17)] were evaluated by averaging values at old and new times, leading to an implicit scheme. The numerical scheme can incorporate either linear or nonlinear drag. For linear drag, numerical solutions converge to the analytic solutions given below. For nonlinear drag, it is neither physically reasonable nor numerically desirable for $\tilde{u}$ to drop to exactly zero (Trowbridge and Madsen, 1984), so we replaced $\tilde{u}$ in (17) with the maximum of $\tilde{u}$ and 0.1. Stem motion was simulated for thirty periods for stems with round cross-section and constant diameter, and the last period of motion was selected for presentation below. We chose $t = 0$ to coincide with the start of this last period, so that $t = 1$ at the end of the last period.

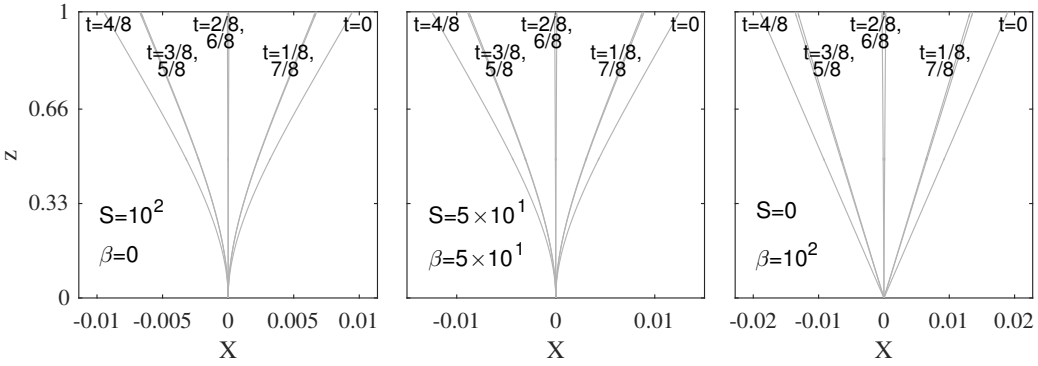

Figure 2: Variation with time t through one wave cycle of horizontal stem displacement X versus elevation z for three nearly-immobile cases. Forces resisting bending are elastic (left), buoyant (right) and mixed (center).

As expected, when either $S \gg 1$ or $\beta \gg 1$, stem motions were much smaller than water motions (so $|X| \ll 1$, Figure 2). Water velocity and stem displacement were maximum in the positive x direction at $t = 0$ or 1, whereas water velocity and stem displacement were maximum in the negative x direction at $t = 1/2$. At $t = 1/4$ and $3/4$ water velocity was zero, and stem displacement was nearly zero. Since water velocity leads water displacement by 1/4 of a cycle, it follows that stem displacement leads water displacement by about 1/4 of a cycle in these nearly-immobile cases (this phase lead is discussed in the context of the elasticity-dominated case by MH10).

Water motions are perfectly sinusoidal with frequency ω, but nonlinearity of the drag formulation leads to small stem motions at odd harmonic frequencies such as 3ω and 5ω (nonlinear friction does not generate even harmonics, see Trowbridge and Madsen, 1984), but the frequency-ω motion accounted for $> 96\%$ of variance in all cases considered here (not shown). Given this dominance of frequency-ω motion, the relationship between water and stem motions is conveniently summarized by the elevation-dependent transfer function

$$\Gamma = \frac{\hat{X}}{\hat{W}}, \tag{30}$$

where the frequency-ω complex amplitudes for stem and water displacement, respectively $\hat{X}$ and $\hat{W}$, were calculated from the final period of simulated motion by complex demodulation [i.e. $\hat{X} = 2\int_0^1 X(t)e^{-i\omega t}\,dt$ and

$\hat{W} = 2\int_0^1 W(t)e^{-i\omega t}\,dt]$. Positive (negative) real Γ indicates stem motion in (out of) phase with water motion, whereas positive (negative) imaginary Γ indicates stem motion leading (lagging) water motion. For immobile stems $\Gamma = 0$, whereas in regions where stems move with surrounding water $\Gamma = 1$. For the nearly-immobile stems shown in Figure 2, which move 1/4-cycle ahead of surrounding water, Γ is small and imaginary (solid black and grey curves Figure 3a-c).

In cases with non-zero S, stem tilt tends smoothly to zero as the bed is approached (Figure 3a-b), whereas non-zero tilt is maintained even close to the bed for $S = 0$ (Figure 3c). Below, it will be shown that stem tilt is small in a near-bed region whose thickness approaches zero when S approaches zero (Section 5).

Numerically-derived transfer functions for a range of stiffness and buoyancy values are shown as solid curves in Figure 3a-i. As stems become more mobile, the component of stem motion in phase with water motion grows larger (increasing positive real component of Γ), until the in-phase and in-quadrature components are of similar size for order-one S or B (compare black and grey curves, Figure 3d-f). For S and B well below 1, the upper parts of stems move almost with surrounding water (Γ approaches 1, Figure 3g-i). As will be discussed further in Section 5, the nearbed region where water and stem motions appreciably differ (i.e. where Γ is substantially different from 1) becomes steadily thinner with decreasing S and β.

4.2. Linearized drag

In this section, analytic solutions to (17), (22) – (25) are presented for the case of linearized drag. These analytic solutions will approximate the numerical solutions for nonlinear drag (Section 4.1), and will clarify scaling.

Consider sinusoidal motion, so $W = (\hat{W}e^{i\omega t} + cc)/2$ and $X = (\hat{X}e^{i\omega t} + cc)/2$, where cc indicates the complex conjugate of the previous term. For stems with round cross-section and constant diameter [so $I = \pi/4$ and $\mathcal{V} = \pi(1-z)$], collecting coefficients of $e^{i\omega t}$ in (17) with linearized drag yields

$$S'\left(\frac{\partial^4\Gamma}{\partial z^4}\right) - \beta'\frac{\partial}{\partial z}\left[(1-z)\frac{\partial\Gamma}{\partial z}\right] = i(1-\Gamma), \tag{31}$$

where

$$S' = 3\pi S/(64\xi), \tag{32}$$

$$\beta' = 3\pi\beta/(16\xi), \tag{33}$$

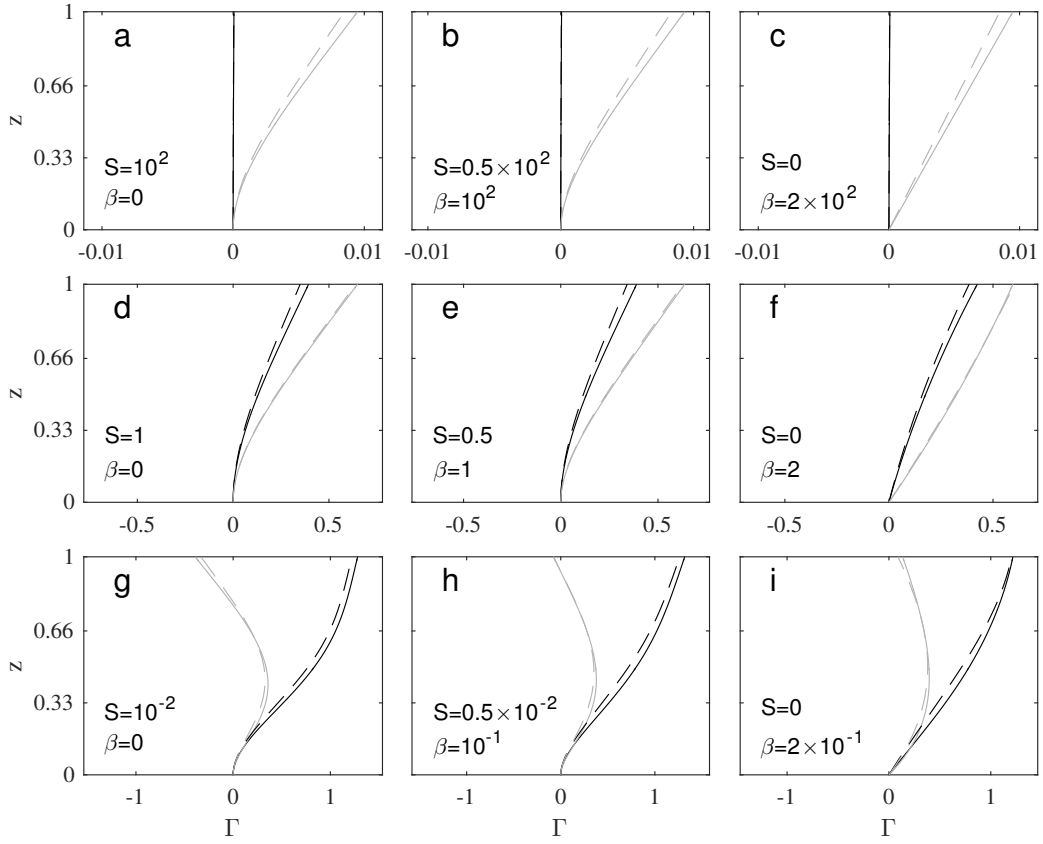

Figure 3: Nonlinear numerical solutions (solid curves) and linearized approximations (dashed curves) for real (black) and imaginary (grey) components of transfer function Γ (defined in equation 30) versus elevation z. Dimensionless stiffness S and buoyancy β, stated in each panel, include (a – c) low-, (d – f) moderate-, and (g – i) high-flexibility cases. Restoring forces elasticity-dominated (a, d, g), buoyancy-dominated (c,f,i), or mixed (b,e,h).

and we have used $\omega = 2\pi$ and $\partial(e^{i\omega t})/\partial t = i\omega e^{i\omega t}$. Boundary conditions are obtained by replacing X with Γ in (22) – (25).

First consider the elasticity-dominated case. Setting $\beta = 0$ recovers the problem considered by MH10, for the special case of depth-uniform water velocity. The solution is

$$\Gamma = 1 - \left(x_1 e^{ir_- z} + x_2 e^{ir_+ z} + x_3 e^{-ir_- z} + x_4 e^{-ir_+ z}\right), \tag{34}$$

where $r_\pm = -[\pm(-i/S')^{1/2}]^{1/2}$ The coefficients $x_1 - x_4$ are determined from the boundary conditions, which yield the system of simultaneous equations

$$A\mathbf{x} = \mathbf{b} \tag{35}$$

where $\mathbf{x} = [x_1, x_2, x_3, x_4]^T$, $\mathbf{b} = [1, 0, 0, 0]^T$, and

$$A = \begin{bmatrix} 1 & 1 & 1 & 1 \\ r_- & r_+ & -r_- & -r_+ \\ r_-^2 e^{r_-} & r_+^2 e^{r_+} & r_-^2 e^{-r_-} & r_+^2 e^{-r_+} \\ r_-^3 e^{r_-} & r_+^3 e^{r_+} & -r_-^3 e^{-r_-} & -r_+^3 e^{-r_+} \end{bmatrix}. \tag{36}$$

Now consider the buoyancy-dominated case. Setting $S = 0$ gives a solution

$$\Gamma = 1 - \frac{J_0\{2[-i\beta'^{-1}(1-z)]^{1/2}\}}{J_0\{2[-i\beta'^{-1}]^{1/2}\}}, \tag{37}$$

where J_0 is a Bessel function of the first kind of order zero. Since (31) reduces to a second-order differential equation in this $S = 0$ case, only two boundary conditions can be satisfied (conditions are (22), and that $\Gamma|_{z=1}$ is finite).

For cases with S and β both nonzero, (31) with linear drag was solved numerically.

The parameter ξ in expression (3) for linearized drag was chosen to minimize the errors resulting from linearization. Agreement between linear and nonlinear drag formulations was optimized using the empirical formula

$$\xi = \frac{1}{2}\left[1 + \frac{4S + \beta^2}{0.2 + 4S + \beta^2}\right]. \tag{38}$$

This expression gives $\xi = 1$ for rigid stems, whereas ξ drops below 1 as stems become flexible, as expected [see discussion following (3)]. The choice of ξ has only a modest effect on solutions, because ξ in (38) never drops below 1/2

(for the flexible limit), and because ξ appears in solutions as only a rescaling of the vertical axis by a constant $\xi^{1/4}$ or $\xi^{1/2}$ [for elasticity- and buoyancy-dominated cases respectively, from (32), (33), (34) and (37)]. Using (38) to evaluate ξ, solutions for linearized drag were found to provide a good approximation to numerical solutions for nonlinear drag (compare solid and dashed curves, Figure 3a-i).

5. Boundary layers

For sufficiently small S and β, the nearbed region where Γ departs appreciably from 1 becomes a thin SBL. A boundary layer coordinate appropriate for negligible buoyancy is (MH10)

$$\zeta_e = \frac{z}{S'^{1/4}}. \tag{39}$$

This coordinate is chosen so that (for $\beta \approx 0$), $\Gamma \approx 0$ for $\zeta_e \ll 1$ and $\Gamma \approx 1$ for $\zeta_e \gg 1$. A boundary layer coordinate appropriate for negligible stiffness will prove to be

$$\zeta_b = \frac{z}{\beta'^{1/2}}. \tag{40}$$

We first express the SBL solution, accounting for both buoyancy and stiffness, as a function of ζ_e, and then note how this solution can be rescaled in terms of ζ_b in the buoyancy-dominated case.

In the SBL, $1 - z \approx 1$, so (31) simplifies to

$$\left(\frac{\partial^2 \Gamma}{\partial \zeta_e^4}\right) - \gamma' \left(\frac{\partial^2 \Gamma}{\partial \zeta_e^2}\right) = i(\Gamma - 1), \tag{41}$$

where the importance of buoyancy relative to stiffness is determined by $\gamma' = \beta' S'^{-1/2}$. Boundary conditions at the bed are unchanged. Far above the bed, stems must move with the surrounding water, so

$$\left.\frac{\partial^2 \Gamma}{\partial \zeta_e^2}\right|_{\zeta_e \to +\infty} = 0, \tag{42}$$

$$\left.\frac{\partial^3 \Gamma}{\partial \zeta_e^3}\right|_{\zeta_e \to +\infty} = 0. \tag{43}$$

The solution is

$$\Gamma = 1 - \frac{r_+ e^{r_- \zeta_e} - r_- e^{r_+ \zeta_e}}{r_+ - r_-}, \tag{44}$$

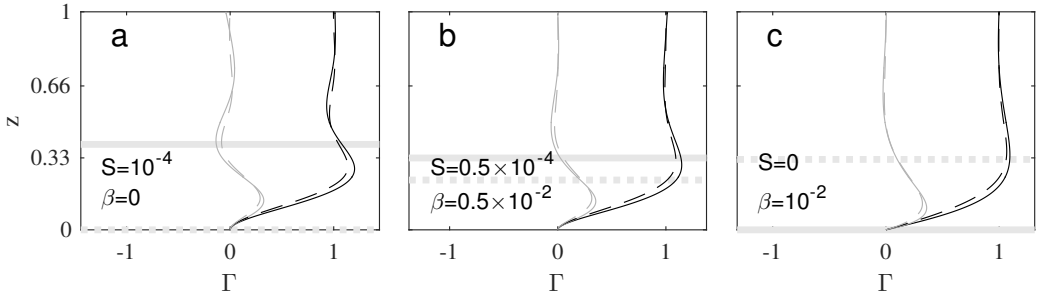

Figure 4: Nonlinear numerical solutions (solid curves) and linearized boundary layer approximations (dashed curves) for real (black) and imaginary (grey) components of transfer function Γ versus elevation z. The small values of dimensionless stiffness S and buoyancy β, stated in each panel, indicate highly flexible stems. Restoring forces elasticity-dominated (a), buoyancy-dominated (c), or mixed (b). Horizontal grey solid and dashed lines respectively mark $z = 3.92S^{1/4}$ and $z = 3.63\beta^{1/2}$.

where

$$r_{\pm} = -\left\{\gamma'/2 \pm [(\gamma'/2)^2 - i]^{1/2}\right\}^{1/2}. \tag{45}$$

For small, moderate, and large γ', these solutions are shown as a function of z (using 39) by dashed lines in Figure 4a – c. In the case presented, the SBL occupies a substantial fraction of the stem. Although (42) – (43) are only formally valid when the SBL is very thin, the SBL solution still provides a good approximation to the numerical solution in the cases shown. With further reductions in S or β, the SBL thickness decreases, and the accuracy of the boundary layer approximation improves further. Near the bed, stem motions lead water motions by 45 °.

For the elasticity-dominated case $\gamma' \ll 1$ (Figure 4a), $r_{\pm} \approx \{e^{i7\pi/8}, e^{-i5\pi/8}\}$, giving a corrected form of the stem boundary layer solution found by MH10 (they erroneously reported $r_{\pm} = \{e^{-i7\pi/8}, e^{-i5\pi/8}\}$). As noted by MH10, the dimensional thickness of this elastic SBL is order $S^{1/4}l_*$. To remove ambiguity, we define the SBL thickness as the elevation where $|\Gamma|$ is maximum, which proves to be $\zeta_e = 3.92$, or $z = 3.92S'^{1/4}$ (solid horizontal grey lines, Figure 4).

For $\gamma' = 1$ (Figure 4b), both buoyancy and stiffness influence leading order stem motion, and the boundary layer thickness remains $O(S^{1/4}l_*)$, which now also equals $O(\beta^{1/2}l_*)$.

For the buoyancy-dominated case $\gamma' \gg 1$ (Figure 4c), $r_+ \approx -\gamma'^{1/2}$ and

$r_- \approx \gamma'^{-1/2} e^{-i3\pi/4}$. From (44) and (40), since $|r_{+*}| \gg |r_{-*}|$,

$$\Gamma \approx 1 - e^{r-\zeta_e} = 1 - e^{r_b \zeta_b}, \tag{46}$$

where $r_b = e^{-i3\pi/4}$. We again define the SBL thickness as the elevation where $|\Gamma|$ is maximum, which occurs at $\zeta_b = 3.23$, or $z = 3.23\beta'^{1/2}$ (dashed horizontal grey lines, Figure 4).

Although the small term omitted from (46) has little effect on X for $\gamma \gg 1$, it does substantially influence $\partial X/\partial z$ in an inner boundary layer. This inner boundary layer is much thinner than the buoyant boundary layer, and is required to satisfy (23). Within this inner layer of thickness $O(\gamma^{-1/2} S^{1/4} l_*) = O[(S/\beta)^{1/2} l_*]$, both buoyancy and stiffness are significant. Although this thin inner boundary layer has little effect on stem displacement or wave dissipation, it may have biological relevance since it influences the stresses exerted on the plant.

6. Approximation of total wave dissipation

The mean depth-integrated wave dissipation is the vertical integral of $\overline{u_* f_{D*}}$, where the overbar ($\overline{\ }$) denotes a time average. This proves to equal the vertical integral of $\overline{(u_* - u_{s*}) f_{D*}}$ (Appendix A). Using this result, for constant diameter stems and depth-uniform flow, the mean depth-integrated dissipation can be written

$$D_* = \alpha D_{r*} \tag{47}$$

where the dissipation for a rigid stem is $D_{r*} = [4/(3\pi)] l_* r_* \rho_* C_D u_{0*}^3$ [the factor $4/(3\pi)$ is the mean of $|\cos^3(t)|$], and the reduction in dissipation resulting from stem motion is measured by

$$\alpha = (3\pi/4) \int_0^1 \overline{|u - u_s|^3}\, dz \tag{48}$$

(in the notation of Luhar and Nepf, 2016, $\alpha = l_e/l$). Note $\alpha = 1$ for rigid stems ($u_s = 0$), whereas $\alpha \ll 1$ indicates a major reduction in dissipation, as expected for highly flexible stems ($u_s \approx u$ along most of stem length).

Dependence of α on S and β, evaluated by repeated numerical simulations with nonlinear drag, is shown in Figure 5. For large S or β, vegetation is almost immobile, dissipation almost equals the rigid-stem value, and $\alpha \approx 1$. Lower S and β result in reduced dissipation and $\alpha < 1$. For $S, \beta \ll 1$, $|u - u_s| \approx 0$ above the SBL, so dissipation scales with the SBL thickness (i.e.

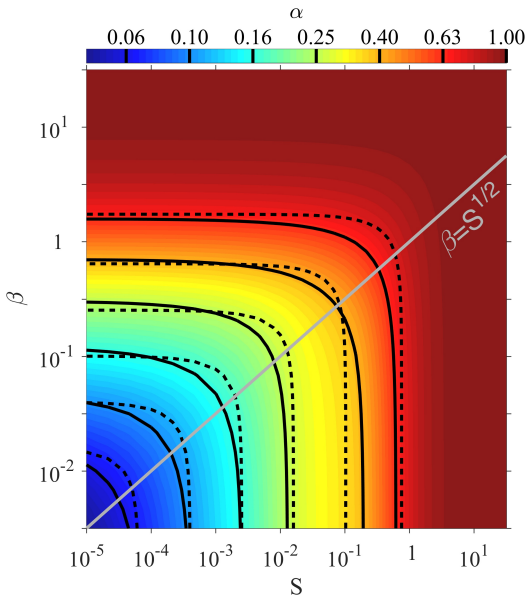

Figure 5: Dimensionless depth-integrated wave dissipation α =(dissipation for flexible stem)/(dissipation for equivalent rigid stem), versus stiffness S and buoyancy β. Color and solid contours: Numerical simulations. Dashed contours: approximate empirical formula (49) (the α value corresponding to each dashed contour equals the α value of the closest solid contour). Buoyancy dominates over elasticity above and to the left of the grey line marking $\beta = S^{1/2}$, whereas elasticity dominates over buoyancy below and to the right. [can be greyscale for print version]

with $S^{1/4}$ when $\beta = 0$, or with $\beta^{1/2}$ when $S = 0$). Across the full range of S and β, the empirical function

$$\alpha \approx \left[\frac{C_S S + C_\beta \beta^2}{1 + C_S S + C_\beta \beta^2} \right]^{1/4} \tag{49}$$

with $C_S = 1/4$ and $C_\beta = 1/16$ approximated α to within 20% (compare solid and dashed contours, Figure 5). This expression was chosen because of it's simplicity, and because it recovers the correct limiting behaviours [i.e. if $S \gg 1$ or $\beta \gg 1$ (rigid limit) then $\alpha \approx 1$; if $S \ll 1$ and $S^{-1/2}\beta \ll 1$ (elastic boundary layer) then $\alpha = O(S^{1/4})$; if $\beta \ll 1$ and $S^{-1/2}\beta \gg 1$ (buoyant boundary layer) then $\alpha = O(\beta^{1/2})$].

We have presented results for cylindrical stems in terms of S and β, but for more complex geometries $\tilde{S}$ and $\tilde{\beta}$ are preferred. Noting that $S =$

$(4/\pi)\tilde{S}$ and $\beta = \tilde{\beta}/\pi$ for cylindrical stems, (49) can be rewritten as $\alpha = [(\tilde{C}_S\tilde{S} + \tilde{C}_\beta\tilde{\beta}^2)/(1 + \tilde{C}_S\tilde{S} + \tilde{C}_\beta\tilde{\beta}^2)]^{1/4}$ where $\tilde{C}_S = 4C_S/\pi = \pi^{-1}$ and $\tilde{C}_\beta = C_\beta/\pi^2 = (4\pi)^{-2}$. This expression is used below to estimate dissipation for stems with rectangular cross section. For stems with complex elevation-dependent geometries, recalculation of numerical solutions would be required.

7. Applications to natural vegetation

The drag coefficient C_D varies with R_e and K_c (Luhar and Nepf, 2016), but for simplicity we will use a typical constant value $C_D = 2$. We also use a seawater density $\rho_* = 1010\,\mathrm{kgm}^{-3}$.

First, we analyze the bending of *Zostera marina* seagrass, whose properties are taken from Luhar and Nepf (2011). We consider stems of length $l_* = 0.4\,\mathrm{m}$ with rectangular cross-section (width normal to flow=8 mm, thickness in flow direction=0.35 mm), density $\rho_{s*} = 700\,\mathrm{kgm}^{-3}$, and Young's modulus $E_* = 10^9\,\mathrm{Pa}$. We assume wave orbital motions with period $t_{0*} = 2\,\mathrm{s}$ and amplitude $u_{0*} = 0.3\mathrm{ms}^{-1}$. For moderately flexible stems, stem tilt is or order (horizontal water particle displacement)/(stem length)$= W_{0*}/(2\pi l_*) = (2\pi L)^{-1} = 0.24$, so stem tilt is only moderately small. Much larger u_{0*} or t_{0*}, as might be common on exposed coasts, would bring the small-tilt approximation into question. The dimensionless stiffness $\tilde{S} = 9.2 \times 10^{-4}$ and the dimensionless buoyancy $\tilde{\beta} = 1.8 \times 10^{-2}$. These values suggest stems slightly less flexible than shown in Figure 4, but substantially more flexible than shown in Figure 3g-i. For steady $0.3\,\mathrm{ms}^{-1}$ flows, buoyancy plays a major role resisting stem bending ($B \sim 20$, Luhar and Nepf, 2011). However, for fluctuating flows the small $\tilde{S}$ and $\tilde{\beta}$ suggest concentration of bending near the bed, which increases the relative importance of elastic forces (because elastic forces scale with a higher vertical derivative). Consequently, the relative importance of buoyancy and elasticity in the SBL is given by $\tilde{\gamma} = \tilde{S}^{-1/2}\tilde{\beta} = 0.58$, indicating a small but non-negligible role for buoyancy. Direct calculation confirms that elasticity is slightly more important than buoyancy for this case [evaluating first and second terms on left of (17) from model output and calculating the root-mean-squared (rms) over all elevations and times yields rms buoyant forcing = 0.49×rms elastic forcing]. Owing to the high flexibility of these stems, predicted dissipation is reduced to 13% of the value expected for equivalent rigid vegetation [i.e. $\alpha = 0.1311$, calculated from (49)]. Neglecting buoyancy would have negligible effect on predicted dissipation ($\alpha = 0.1308$ if buoyancy is neglected), whereas neglecting elasticity

would lead to substantial errors ($\alpha = 0.037$ if elasticity is neglected).

Next consider the seagrass *Thalassia testudinum*. Plant properties (from Bradley and Houser, 2009; Luhar and Nepf, 2011) are $l_* = 0.225\,\mathrm{m}$, width=10 mm, thickness=0.35 mm, $E = 2.4 \times 10^9\,\mathrm{Pa}$, and $\rho_{s*} = 942\,\mathrm{kgm^{-3}}$. Applying the same wave conditions as used above for Z. marina ($t_{0*} = 2\,\mathrm{s}$, $u_{0*} = 0.3\mathrm{ms^{-1}}$) yields $L = 0.38$, $\tilde{S} = 0.011$, $\tilde{\beta} = 0.0041$ (resembling the case of Figure 3g), and $\alpha = 0.22$. *T. testudinum* dimensionless stiffness exceeds that of *Z. Marina* mainly because of the shorter *T. testudinum* stem length [from (20), S is proportional to l_*^{-4}; *T testudinum's* higher Young's modulus also played a role]. For steady flows $B = 0.38$, indicating a small but non-negligible role for buoyancy. In contrast, $\tilde{\gamma} = 0.039$, suggesting that buoyancy plays very little role under unsteady wave orbital velocities. This is confirmed by direct numerical evaluation of elastic and buoyant forces (rms buoyant force = 0.047×rms elastic force). Next consider lower-energy waves ($u_{0*} = 0.02\mathrm{ms^{-1}}$, $t_{0*} = 1.33\,\mathrm{s}$), comparable to those observed in the field by Bradley and Houser (2009). Now $L = 8.5$, $\tilde{S} = 0.11$, $\tilde{\beta} = 0.041$, $\alpha = 0.40$. Owing to the greatly reduced drag in these lower energy conditions, stems are now able to resist bending more effectively. Given observed stem density (1100 stems/m^2) and depth (1 m), modifying a standard formula for attenuation of waves propagating over a rigid canopy (Henderson et al., 2017) to reduce dissipation by the factor $\alpha = 0.40$ yields the prediction that waves propagate a distance $x_{0*} = 67\,\mathrm{m}$ before their height is halved. This is in agreement with the observed $x_{0*} = 54 - 103\,\mathrm{m}$ (inferred from Figure 2 of Bradley and Houser, 2009), although uncertainty about vegetation properties precludes a more rigorous test.

MH10 simulated dissipation by the sedge *Schenoplectus americanus*, with typical $l_* = 0.6\,\mathrm{m}$, $r_{0*} = 2\,\mathrm{mm}$, $E_* = 3 \times 10^8\,\mathrm{Pa}$, $t_{0*} = 2\,\mathrm{s}$, and $u_{0*} = 0.1\,\mathrm{ms^{-1}}$. Assuming $\rho_{s*} = 700\,\mathrm{kgm^{-3}}$, it follows that $S = 0.18$ and $\beta = 0.1$. For such moderate flexibility stems, bending is not confined to a SBL, but instead extends along the stem's full length. It follows that the ratio of buoyant and elastic terms is not $\gamma = S^{-1/2}\beta$, as it would be in the SBL limit, but instead is of order $S^{-1}\beta = B = 0.56$. Direct calculation confirms a small but non-negligible role for buoyancy (rms buoyant term 0.33×rms elastic term). Therefore, the MH10 assumption of negligible buoyancy may not be justified for this case. However, a small buoyant force does not greatly modify stem behaviour (e.g. compare Figure 3e,f), likely explaining the good fit between observed stem bending and the elastic theory found by MH10 (an error in the MH10 estimate of E_*, which was chosen to fit observations, is likely).

Buoyancy also has little effect on dissipation: $\alpha = 0.434$ for the observed S and β, whereas $\alpha = 0.432$ if β is reset to zero. For the observed stem densities (about 300 stems/m^2), these α values are consistent with observed attenuation of waves propagating through the sedge canopy (Riffe et al., 2011).

Pneumatophores of the mangrove *Sonertia alba* provide an example of nearly rigid stems. We assume $t_{0*} = 2\,\mathrm{s}$, $u_{0*} = 0.3\,\mathrm{ms}^{-1}$, $l_* = 0.15\,\mathrm{m}$, $r_{0*} = 5\,\mathrm{mm}$, $E_* = 8 \times 10^9\,\mathrm{Pa}$, and $\rho_{s*} = 660\,\mathrm{kgm}^{-3}$ (Zhang et al., 2015). Now $L = 0.25$ and $(2\pi L)^{-1} = 0.64$, suggesting that the small tilt approximation would not be very accurate if stems were very flexible. However, owing to near-rigidity ($S = 6.5 \times 10^3$, $\beta = 0.37$), predicted $l_*/(\text{maximum } X_*) = 1.6 \times 10^3$, so tilt is small.

The giant kelp *Macrocystis pyrifera* provides an example of a buoyancy-dominated case. Since these plants grow in coastal environments exposed to energetic long-period waves we take $t_{0*} = 12\,\mathrm{s}$, $u_{0*} = 1.0\,\mathrm{ms}^{-1}$. Neglecting complex geometry, we model fronds as cylinders with $l_* = 15\,\mathrm{m}$, $r_{0*} = 1\,\mathrm{cm}$, $E_* = 1 \times 10^7\,\mathrm{Pa}$, and $\rho_{s*} = 595\,\mathrm{kgm}^{-3}$ (these properties chosen for consistency with Utter and Denny, 1996, with artificially low ρ_{s*} chosen to yield a total buoyant force equal to the combined buoyant force of realistic stems and pneumatocysts). For this highly flexible case ($S = 1.2 \times 10^{-6}$, $\beta = 1.6 \times 10^{-2}$) with $\gamma = 15$, a buoyancy-dominated SBL is expected to extend about $3.23\beta^{1/2} l_* = 6.1\,\mathrm{m}$ above bed. The low S and β partly result from the long stem length, with the exceptionally low Young's modulus also playing a role (Koehl and Wainwright, 1977). For cylindrical stems, elastic forces would become important within an inner boundary layer extending about $(S/\beta)^{1/2} l_* = 0.13\,\mathrm{m}$ above the bed. However, within this small distance of the bed the cylindrical approximation may become inaccurate, as stems spread to form a wide holdfast with complex geometry. Since $L = 1.25$, stem tilt would be small [order $(2\pi L)^{-1} = 0.13$] if bending were spread along the full length of the stem. However, bending is in fact concentrated within the SBL, where tilt is about $u_{0*}t_{0*}/[2\pi(\text{SBL thickness})] = 0.31$. Therefore, much greater $u_{0*}t_{0*}$ would violate the small-tilt approximation. For these highly flexible stems $\alpha = 0.05$, consistent with the minimal dissipation observed in the field (Elwany et al., 1995).

Mullarney and Pilditch (2017) measured tilts along the lengths of *M. pyrifera* stems exposed to natural waves, with $u_{0*} \approx 0.2\,\mathrm{ms}^{-1}$, $l_* = 2.2\,\mathrm{m}$, dominant swell period $t_{0*} = 9\,\mathrm{s}$ (other kelp properties taken as above). Resulting $S = 9.5 \times 10^{-3}$, $\beta = 0.41$ and $\alpha = 0.34$, so we expect a buoyancy-

dominated, partially flexible case resembling Figure 3i, with relatively large stem tilts near the bed. Near the stem's free end, measured tilts often exceeded 90° from vertical, possibly owing to proximity of the water surface, so results from the uppermost instrument will be excluded from the following discussion. Among remaining measurement locations, at swell periods, stem tilts were greatest near the bed, consistent with theory. Conversely, at longer infragravity periods (nominally 64 s), tilt fluctuations were relatively uniform along the stem, with a slight reduction near the bed (excluding the topmost sensor). To explain this observation, we re-consider scaling for the case of a low-energy infragravity-frequency motion in the presence of more energetic swell. We redefine u_{0*}, t_{0*} and W_{0*} to be representative of infragravity motions. Scaling now proceeds as in Section 2, with the exception of $\tilde{u}_*$, which is scaled by the amplitude of the dominant swell-frequency motion (following Lowe et al., 2007; Mullarney and Henderson, 2010). Analysis then yields $S_{ig} = (t_{ig*}/t_{sw*})S$ and $\beta_{ig} = (t_{ig*}/t_{sw*})\beta$, where t_{ig*} and t_{sw*} are respectively infragravity and swell periods, S and β are dimensionless stiffness and buoyancy for swell frequency motions (as calculated above), and S_{ig} and β_{ig} are dimensionless stiffness and buoyancy for infragravity frequency motions. Resulting $S_{ig} = 6.8 \times 10^{-2}$ and $\beta_{ig} = 3$, suggesting low-frequency behaviour resembling Figure 3f (although stiffness may not be entirely negligible, causing a small reduction in near-bed tilts). Predicted infragravity tilt fluctuations are non-longer maximum near the bed, consistent with observations. Flexibility of blades attached to the 'stypes' (i.e. the primary stems), neglected here, may also influence the observed behaviour (Mullarney and Pilditch, 2017). Nevertheless, the observed qualitative frequency-dependence of kelp tilts is consistent with the simple analysis presented above. This case also illustrates the importance of low frequency motions to stem displacement and dissipation (c.f. Stevens et al., 2001). Since $\beta_{ig} > \beta$, the model predicts that the ratio (stem displacement)/(water particle displacement) is smaller at infragravity frequencies than at incident frequencies. However, since water particle displacements depend on frequency, this does not imply that infragravity stem displacements are smaller than incident-frequency stem displacements. Incident waves were an order of magnitude more energetic than infragravity waves, but water particle displacements scale with velocity×period, and displacements of water particles at long infragravity periods ($\sim$ 6 m) were larger than displacements at shorter swell periods (~ 0.3 m). Consequently, although $\beta_{ig} > \beta$, the predicted infragravity-period stem displacement ($\sim 6\,\mathrm{m}/\beta_{ig} = 2$ m) exceeds the predicted swell-period stem

displacement ($\sim 0.3\,\mathrm{m}$, using Figure 3i). These predictions are consistent with observations of order-one stem tilt fluctuations at infragravity periods, with smaller fluctuations at incident periods.

Assumptions of depth-uniform flow and small stem tilt were adopted in the above discussion. These assumptions are examined in Appendix B and Appendix C.

Although the above discussion focused on positive buoyancy as a factor preventing stem bending, the model equations remain applicable for plants with negative buoyancy (e.g. some *Turbinaria ornata*, Stewart, 2006), so long as stiffness is sufficient to prevent large stem tilts. Comparison with classical analysis of the self-buckling beam problem (Greenhill, 1881) shows that a negatively buoyant stem in still water can support its own immersed weight when $|\beta/S| \ll 1$, but will collapse when $|\beta/S| \gg 1$ (note $|\beta/S| = |B|$).

8. Summary and Discussion

The model (17) can simulate stem motion and wave dissipation for a variety of stem geometries and depth-dependent flows. However, to highlight qualitative behaviour and emphasize key dimensionless parameters, analysis here has focused on the simple case of constant-diameter stems in depth-uniform flows. The model, representing a balance of elasticity, buoyancy and drag, predicts bending along the length of a stem. Predicted stem motion depends on hydrodynamic parameters (amplitude and period of velocity fluctuations) and stem properties (the stem's Young's modulus, density, length, and radius). A key result is that the ratio between water and stem displacements is controlled by new dimensionless buoyancy parameter β (equations 21 and 19), in addition to the stiffness parameter S (equations 20 and 18) considered by previous researchers. When $S \gg 1$ or $\beta \gg 1$ stems move much less than surrounding water particles (Figure 3a–c), whereas stem and water motions become comparable where S and β are order-one (Figure 3d–f). For $S \ll 1$ and $\beta \ll 1$ stems are highly flexible, with stem bending concentrated near the seabed (Figures 3g–h and 4a–c). In such highly flexible cases, the relative magnitude of buoyant and elastic forces scales with $S^{-1/2}\beta$ (Section 5). For the simple cases simulated, closed-form algebraic expressions (47), (49) provide a good approximation of mean depth-integrated wave dissipation across the full range of β and S. These expressions are sufficiently simple for application to field cases, or for incorporation in wave propagation models. Application to a range of natural vegetation suggests a small

role for buoyancy in some seagrasses and sedge cases, and (as expected) a dominating role for buoyancy in giant kelp (Section 7).

Key model assumptions include large Keulegan-Carpenter number and small stem tilt. The large Keulegan-Carpenter number condition is usually met by highly flexible stems. Some cases satisfy the small-tilt approximation, such as giant kelp under moderate waves, and many seagrasses under the short-period low-energy waves common in estuaries. In contrast, large tilts will be more frequent for smaller kelp, and for both seagrasses and giant kelp under some higher-energy conditions. For the case of negligible buoyancy, previous observations (Luhar et al., 2017; Luhar and Nepf, 2016; Mullarney and Henderson, 2010; Riffe et al., 2011) have established model skill, even in cases where tilts are not small. For the buoyancy-dominated case, model predictions are qualitatively consistent with existing field observations of kelp motion (Mullarney and Pilditch, 2017), but further experiments will be required to develop more quantitative tests of model accuracy.

The theoretical range of applicability of the theory developed here, and its relationship to previous work, is summarized in table 2. The theory developed here applies for most cases with large dimensionless length L (which usually corresponds to small tilt cases), whereas previous steady-flow analysis (Luhar and Nepf, 2011) may apply for cases with small L (Luhar and Nepf, 2016). Therefore, simple dissipation scalings, applicable for any combination of buoyancy and elasticity, have now been developed for both small- and large-L limits. For transitional cases with $L \sim 1$, further work will be required to determine whether behaviour is intermediate between large- and small-L cases, or whether new physics will arise. Additional work may also be required to develop models for vegetation with complex, branching geometry. Nevertheless, qualitative model predictions were encouraging for the case of giant kelp, despite the contrast between the simple geometry of modeled stems and the complex geometry of the natural vegetation.

Table 1: List of Variables.

Variable	Meaning	Units
A_*	stem cross-sectional area	m^2
$b_* = \frac{g_*(\rho_* - \rho_{s*})}{\rho_*}$	stem buoyancy	ms^{-2}
C_D	stem drag coefficient	–
$C_a = \frac{\rho_* r_{0*} u_{0*}^2 l_*^3}{E_* I_{0*}}$	Cauchy number	–
D_*	depth-integrated mean wave dissipation for flexible stem	$\mathrm{kg\,m^2 s^{-3}}$
D_{r*}	depth-integrated mean wave dissipation for rigid stem	$\mathrm{kg\,m^2 s^{-3}}$
E_*	stem Young's modulus	$\mathrm{kg\,m^{-1} s^{-2}}$
f_{b*}	vertical buoyant force on stem, per unit stem length	$\mathrm{kg\,s^{-2}}$
f_{d*}	horizontal drag force on stem, per unit stem length	$\mathrm{kg\,s^{-2}}$
F_{b*}	vertical buoyant force integrated along length of stem	$\mathrm{kg\,ms^{-2}}$
F_{d*}	horizontal drag force integrated along length of stem	$\mathrm{kg\,ms^{-2}}$
g_*	gravitational acceleration	ms^{-2}
I_*	second moment of stem area	m^4
$I_{0*} = r_{0*}^4$	typical scale for I_{0*}	m^4
$I = I_*/I_{0*}$	dimensionless second moment of stem area	–
l_*	stem length	m
$L = l_*/W_{0*}$	dimensionless stem length	–
$P = \frac{C_D u_{0*}^2}{b_* r_{0*}}$	dimensionless buoyancy (steady flow)	–
r_*	stem radius	m
r_{0*}	stem radius at $z = 0$	m
$r = r_*/r_{0*}$	dimensionless stem radius	–
s_*	distance from stem base, measured along stem	m
$S = \frac{E_* r_{0*}^3 t_{0*}}{\rho_* C_D l_*^4 u_{0*}}$	dimensionless stiffness	–
t_*	time	s
t_{0*}	wave period	s
$t = t_*/t_{0*}$	dimensionless time	–
T	tension, integrated over stem cross-section	$\mathrm{kg\,ms^{-2}}$
u_*	horizontal water velocity	ms^{-1}
u_{s*}	horizontal stem velocity	ms^{-1}
u_{0*}	amplitude of water velocity fluctuations	ms^{-1}
$u = u_*/u_{0*}$	dimensionless water velocity	–
$u_s = u_{s*}/u_{0*}$	dimensionless stem velocity	–
V_*	elastic shear stress, integrated over stem cross-section	$\mathrm{kg\,ms^{-2}}$
$\mathcal{V}_*$	stem volume above elevation z	m^3
$\mathcal{V}_{0*}$	volume of entire stem	m^3
$\mathcal{V} = \mathcal{V}_*/\mathcal{V}_{0*}$	dimensionless stem volume above elevation z	–
W_*	horizontal displacement of water particles	m
$W_{0*} = u_{0*} t_{0*}$	$(2\pi)\times$amplitude of water particle displacement	m
$W = W_*/W_{0*}$	dimensionless water particle displacement	–
X_*	horizontal stem displacement	m
$X = X_*/W_{0*}$	dimensionless stem displacement	–
z_*	elevation above bed	m
$z = z_*/l_*$	dimensionless elevation	–
$\alpha = D_*/D_{r*}$	dimensionless dissipation	–
$\beta = \frac{b_* r_{0*} t_{0*}}{C_D l_* u_{0*}}$	dimensionless buoyancy (oscillatory flow)	–
Γ	ratio between stem and water complex amplitudes	–
ν	kinematic viscosity of water	$\mathrm{m^2 s^{-1}}$
ρ_*	water density	$\mathrm{kg\,m^{-3}}$
ρ_{s*}	stem density	$\mathrm{kg\,m^{-3}}$
θ	stem tilt (radians from vertical)	–

Table 2: Summary of scalings for dissipation under quasi-steady ($L \ll 1$) and small tilt ($L \gg 1$) limits in cases where bending is resisted by elasticity, buoyancy, or both elasticity and buoyancy. Previous theories presented by DE08: de Langre (2008); LN11:Luhar and Nepf (2011); NE98: Nikora et al. (1998); MH10: Mullarney and Henderson (2010). Question marks indicate cases for which no simple scaling has yet been developed.

	$L \ll 1$ quasi-steady	$L \sim 1$ transitional	$L \gg 1$ small tilt
Elastic	DE08	?	MH10
Elastic + Buoyant	LN11	?	This paper
Buoyant	NE98	?	This paper

Acknowledgements

We thank Julia Mullarney for helpful suggestions. This work was funded by the US Office of Naval Research [Littoral Geosciences grant number N000141410112].

Appendix A. Alternative expressions for depth-integrated dissipation

Viewed from a frame of reference moving with the stem, dissipation appears to be $(u_* - u_{s*})f_{D*}$, whereas viewed from a fixed frame, dissipation is $u_* f_{D*}$. We will show that, when depth-integrated and time-averaged, these two expressions are equal for the model used here.

First note that $u_* f_{D*} = (u_* - u_{s*})f_{D*} + u_{s*}f_{D*}$. Therefore, we must show that $\int_0^{l_*} \overline{u_{s*}f_{D*}}\, dz_* = 0$, or in dimensionless variables $\int_0^1 \overline{u_s f_D}\, dz = 0$. Physically, we are showing that no significant mean work is done on the solid, so all dissipation occurs within the water. Here the dimensionless force

$$f_D = r\tilde{u}(u - u_s) = r\tilde{u}\,\partial(W - X)/\partial t \tag{A.1}$$

equals the right of (17). Multiplying both sides of (A.1) by $u_s = \partial X/\partial t$, depth-integrating, time-averaging, and using (17) yields

$$\int_0^1 \overline{u_s f_D}\, dz = D_S + D_\beta, \tag{A.2}$$

where

$$D_S = S\int_0^1 \overline{\frac{\partial X}{\partial t}\frac{\partial^2}{\partial z^2}\left(I\frac{\partial^2 X}{\partial z^2}\right)}\, dz, \tag{A.3}$$

$$D_\beta = -\beta\int_0^1 \overline{\frac{\partial X}{\partial t}\frac{\partial}{\partial z}\left(\mathcal{V}\frac{\partial X}{\partial z}\right)}\, dz. \tag{A.4}$$

It remains to show that $D_S = 0$ and $D_\beta = 0$. Integrating (A.4) by parts yields

$$D_\beta = -\beta\frac{\partial X}{\partial t}\left(\mathcal{V}\frac{\partial X}{\partial z}\right)\Big|_{z=1} + \beta\frac{\partial X}{\partial t}\left(\mathcal{V}\frac{\partial X}{\partial z}\right)\Big|_{z=0} + \beta\int_0^1 \overline{\frac{\partial^2 X}{\partial t\partial z}\left(\mathcal{V}\frac{\partial X}{\partial z}\right)}\, dz. \tag{A.5}$$

The first term is zero because $\mathcal{V}|_{z=1} = 0$, the second term is zero from (22), and the integrand in the third term is

$$\overline{\mathcal{V}\left(\frac{\partial X}{\partial z}\right)\frac{\partial}{\partial t}\left(\frac{\partial X}{\partial z}\right)} = \frac{\mathcal{V}}{2}\overline{\frac{\partial}{\partial t}\left[\left(\frac{\partial X}{\partial z}\right)^2\right]} = 0, \tag{A.6}$$

where the last equality follows from periodicity of the motion.

The result $D_S = 0$ follows in a similar manner after integrating by parts twice and applying boundary conditions.

Appendix B. The depth-uniform flow approximation

Using the cases outlined in Section 7, we examine the accuracy and limitations of the depth-uniform flow approximation. For cases with $t_{0*} = 2\,\mathrm{s}$, even in just 2 m depth, near-bed velocity is smaller than near-surface velocity by a factor of $\cosh(k_* h_*) = 4$, where $h_* =$ water depth and $k_* = 2\pi/$wavelength (here calculated from linear wave theory). In contrast, velocity is attenuated from the top to the bottom of *Z. marina* by only a factor of $\cosh(k_* l_*) = 1.09$ (i.e. 9% attenuation). Therefore, it is important to account for depth-attenuation over the full water depth, but the neglect of vertical attenuation within the canopy is justified. Next consider the *M. prifera* case with a 15-m-long stem, assuming water depth of 16 m, and take $t_{0*} = 9\,\mathrm{s}$. Now $k_* = 0.064\,\mathrm{m}^{-1}$, $\cosh(k_* h_*) = 1.6$, and $\cosh(k_* l_*) = 1.5$, indicating substantial variability over the depth and along length of stem. However, we know from the small S and β values that the stem can easily bend along its full length to accommodate this variability, so substantial differences between water and stem velocities are again confined to an SBL, with the appropriate u_{0*} being the nearbed value (within the SBL, velocity varries only 4%, so the depth-uniform flow approximation is valid). Finally, consider giant kelp with shorter period 3 s waves (holding other factors constant). Now $k_* = 0.45\,\mathrm{m}^{-1}$, and $\cosh(k_* h_*) = 640$, indicating very little nearbed flow since these short waves are essentially in deep water. Since flow in SBL is negligible, scalings based on SBL dissipation are invalid. Flow is almost completely attenuated along length of stem [$\cosh(k_* l_*) = 430$]. Furthermore, the length scale for depth attenuation of flow is now $k_*^{-1} = 2.2\,\mathrm{m}$. Therefore, scaling (7) is inappropriate and the vertical coordinate should be rescaled using the scale k_*^{-1}. Although full analysis is beyond the scope of this paper, we briefly note that such scaling (with $z = k_* z_*$), leads to to modified values

$S = 5 \times 10^{-3}$ and $\beta = 0.16$. Such values indicate that buoyancy, although insufficient to resist bending of the stem along its full length, is sufficient to weakly resist the near-surface bending imposed by the depth-dependent flows of these short period waves. Kelp may therefore allow passage of long period waves while damping short waves (similar behaviour was noted for elastic sedge by MH10). Depth-variability of velocity introduces two new dimensionless parameters (k_*h_* and k_*l_*), and evaluation of the full range of possibilities is beyond scope of this paper. However, we note that cases with depth-dependent flows can be solved numerically, or analytically by representing the vertical structure as a sum of normal modes (adapting approach of MH10 to account for buoyancy).

Appendix C. The small-tilt approximation

The small-tilt approximation will often be justified when $L \gg 1$. Nevertheless, considering the examples of Section 7, the *S. alba* case indicates that $L \gg 1$ is not always necessary for validity of the small tilt approximation, while the *M. pyrifera* case with $l_* = 15\,\mathrm{m}$ and a well-developed stem boundary layer indicates that $L \gg 1$ is not always sufficient. We can generally assess small tilt approximation from known S and β as follows: if $S \gg 1$ and/or $\beta \gg 1$, then tilt is small if $2\pi L \times \max(S, \beta) \gg 1$, [here $\max(A, B)$ denotes the maximum of A and B]. Otherwise, tilt is small if $2\pi L \times \max(3.92S^{1/4}, 3.23\beta^{1/2}) \gg 1$.

References

Arkema, K. K., Guannel, G., Verutes, G., Wood, S. A., Guerry, A., Ruckelshaus, M., Kareiva, P., Lacayo, M., and Silver, J. M. (2013). Coastal habitats shield people and property from sea-level rise and storms. *Nature Climate Change*, 3(10):913–918.

Augustin, L. N., Irish, J. L., and Lynett, P. (2009). Laboratory and numerical studies of wave damping by emergent and near-emergent wetland vegetation. *Coastal Engineering*, 56:332 – 340.

Blackmar, P. J., Cox, D. T., and Wu, W.-C. (2014). Laboratory observations and numerical simulations of wave height attenuation in heterogeneous vegetation. *Journal fo Waterway, Port, Coastal, and Ocean Engineering*, 140:56 – 65.

Borgman, L. (1967). Spectral analysis of wave forces on piling. *Journal of the Waterways and Harbors Division, ASCE*, 93:129 – 156.

Bradley, K. and Houser, C. (2009). Relative velocity of seagrass blades: Implications for wave attenuation in low-energy environments. *J. Geophys. Res.*, 114:doi:10.1029/2007JF000951.

Brander, L., Florax, R. J., and Vermaat, J. E. (2006). The empirics of wetland valuation: A comprehensive summary and a meta-analysis of the literature. *Environmental and Resource Economics*, 33:223 – 250.

Broekx, S., Smets, S., Liekens, I., Bulckaen, D., and De Nocker, L. (2011). Designing a long-term flood risk management plan for the scheldt estuary using a risk-based approach. *Natural Hazards*, 57(2):245–266.

Dalrymple, R. A., Kirby, J., and Hwang, P. (1984). Wave diffraction due to areas of energy dissipation. *Journal of Waterway, Port, Coastal, and Ocean Engineering*, 110:67 – 79, http://dx.doi.org/10.1061/(ASCE)0733–950X(1984)110:1(67).

de Langre, E. (2008). Effects of wind on plants. *Annu. Rev. Fluid Mech.*, 40:141 – 168.

Denny, M. and Gaylord, B. (2002). The mechanics of wave-swept algae. *Journal of Experimental Biology*, 205:1355 – 1362.

Denny, M., Gaylord, B., and Cowen, E. A. (1997). Tflow and flexibility. ii: The roles of size and shape in determining wave forces on the bull kelp *Nereocystis Luetkeana*. *Journal of Experimental Biology*, 200:3165 – 3183.

Denny, M., Gaylord, B., Helmuth, B., and Daniel, T. (1998). The menace of momentum: Dynamic forces on flexible organisms. *Limnol. Oceanogr.*, 43:955 – 968.

Elwany, M. H. S., OReilly, W., Guza, R., and Flick, R. (1995). Effects of Southern California kelp beds on waves. *Journal of Waterway, Port, Coastal, and Ocean Engineering*, 121(2):143 – 150.

Feagin, R. A., Figlus, J., Zinnert, J. C., Sigren, J., Martinez, M. L., Silva, R., Smith, W. K., Cox, D., Young, D. R., and Carter, G. (2015). Going with the flow or against the grain? the promise of vegetation for protecting

beaches, dunes, and barrier islands from erosion. *Frontiers in Ecology and the Enivronment*, 13:203 – 210.

Greenberg, R., Maldonado, J., Droege, S., and Mcdonald, M. (2006). Tidal marshes: a global perspective on the evolution and conservation of their terrestrial vertebrates. *Bioscience*, 56:675 – 685, http://dx.doi.org/10.1641/0006–3568(2006)56[675:TMAGPO]2.0.CO;2.

Greenhill, A. (1881). Determination of the greatest height consistent with stability that a vertical pole or mast can be made, and the greatest height to which a tree of given proportions can grow. *Proc. Cambridge Philos. Soc.*, 4:65 – 73.

Gren, I.-M. (1995). The value of investing in wetlands for nitrogen abatement. *Eur Rev Agric Econ*, 22:157 – 172.

Henderson, S. M., Norris, B. K., Mullarney, J. C., and Bryan, Karin, R. (2017). Wave-frequency flows within a near-bed vegetation canopy. *Continental Shelf Research*, 147:91 – 101, http://dx.doi.org/10.1016/j.csr.2017.06.003.

Jadhav, R. S., Chen, Q., and Smith, J. M. (2013). Spectral distribution of wave energy dissipation by salt marsh vegetation. *Coastal Engineering*, 77:99–107, 10.1016/j.coastaleng.2013.02.013.

Jones, H. P., Hole, D. G., and Zavaleta, E. S. (2012). Harnessing nature to help people adapt to climate change. *Nature Climate Change*, 2:504 – 509.

Kobayashi, N., Rachel, A. W., and Asano, T. (1993). Wave attenuation by vegetation. *J. Waterway Port Coastal Ocean Eng.*, 119:30 – 48.

Koehl, M. (1984). How do benthic organisms withstand moving water? *American Zoologist*, 24(1):57–70.

Koehl, M. and Wainwright, S. (1977). Mechanical adaptations of a giant kelp. *Limnology and Oceanography*, 22:1067 – 1071.

Lowe, R. J., Falter, J. L., Koseff, J. R., Monismith, S. G., and Atkinson, M. J. (2007). Spectral wave flow attenuation within submerged canopies: Implications for wave energy dissipation. *Journal of Geophysical Research: Oceans*, 112(C5):doi:10.1029/2006JC003605. C05018.

Lowe, R. J., Koseff, J. R., and Monismith, S. G. (2005). Oscillatory flow through submerged canopies: 1. velocity structure. *Journal of Geophysical Research*, 110:doi:10.1029/2004JC002788.

Luhar, M., Infantes, E., and Nepf, H. M. (2017). Seagrass blade motion under waves and its impact on wave decay. *Journal of Geophysical Research*, 122:3736 – 3752.

Luhar, M. and Nepf, H. M. (2011). Flow-induced reconfiguration of buoyant and flexible aquatic vegetation. *Limnology and Oceanography*, 55:2003 – 2017, doi:10.4319/lo.2011.56.6.2003.

Luhar, M. and Nepf, H. M. (2016). Wave-induced dynamics of flexible blades. *Journal of Fluids and Structures*, 61:20 – 41, http://dx.doi.org/10.1016/j.jfluidstructs.2015.11.007.

Mendez, F. J. and Losada, I. J. (2004). An empirical model to estimate the propagation of random breaking and nonbreaking waves over vegetation fields. *Coastal Engineering*, 51:103 – 118.

Möller, I., Kudella, M., Rupprecht, F., Spencer, T., Paul, M., van Wesenbeeck, B. K., Wolters, G., Jensen, K., Bouma, T. J., Miranda-Lange, M., and Schimmels, S. (2014). Wave attenuation over coastal salt marshes under storm surge conditions. *Nature Geoscience*, 7:727 – 731.

Morton, K. and Mayers, D. (2005). *Numerical Solution of Partial Differential Equations: An Introduction*. Cambridge, 2 edition.

Mullarney, J. C. and Henderson, S. M. (2010). Wave-forced motion of submerged single stem vegetation. *J. Geophys. Res.*, 115.

Mullarney, J. C. and Henderson, S. M. (2018). Flows within marine vegetation canopies. In *Advances in Coastal Hydraulics*, pages 1 – 46. World Scientific.

Mullarney, J. C. and Pilditch, C. A. (2017). The differential response of kelp to swell and infra gravity wave motion. *Limnology and Oceanography*, 62:2524 – 2537.

Niklas, K. J. (1992). *Plant Biomechanics*. University of Chicago Press.

Nikora, V., Goring, D., and Biggs, B. (1998). A simple model of stream periphyton-flow interactions. *Oikos*, 81:607 – 611.

Riffe, K. C., Henderson, S. M., and Mullarney, J. C. (2011). Wave dissipation by flexible vegetation. *Geophysical Research Letters*, 38:doi:10.1029/2011GL048773.

Rosman, J., Koseff, J., Monismith, S., and Grover, J. (2007). A field investigation into the effects of a kelp forest (Macrocystis pyrifera) on coastal hydrodynamics and sediment transport. *J. Geophys. Res.*, 112:doi:10.1029/2005JC003430.

Siikamäki, J., Sanchirico, J. N., and Jardine, S. L. (2012). Global economic potential for reducing carbon dioxide emissions from mangrove loss. *Proceedings of the National Academy of Sciences of the United States of America*, 109(36):14369–14374.

Simmons, G. F. (1972). *Differential equations : with applications and historical notes*. McGraw-Hill, New York, 1 edition.

Stevens, C., Hurd, C., and Smith, M. (2001). Water motion relative to subtotal kelp fronds. *Limnol. Oceanogr.*, 46:668 – 678.

Stewart, H. L. (2006). Morphological variation and phenotypic plasticity of buoyancy in the macroalga *Turbinaria ornata* across a barrier reef. *Marine Biology*, 149:721 – 730.

Sumer, B. and Fredsøe, J. (1997). *Hydrodynamics Around Cylindrical Structures*. Advanced Series in Applied Physics. World Scientific.

Temmerman, S., Meire, P., Bouma, T., Herman, P., Ysebaert, T., and De Vriend, H. (2013). Ecosystem-based coastal defence in the face of global change. *Nature*, 504:79 – 83, doi:10.1038/nature12859.

Trowbridge, J. and Madsen, O. (1984). Turbulent wave boundary layers 1. model formulation and first-order solution. *J. Geophys. Res.*, 88:7989–7997.

Utter, B. D. and Denny, M. W. (1996). Wave-induced forces on the giant kelp Macrocystis pyrifera (AGARDH): Field test of a computational model. *Journal of Experimental Biology*, 199:2645 – 2654.

Zeller, R. B., Weitzman, J. S., Abbett, M. E., Zarama, F. J., Fringer, O. B., and Koseff, J. R. (2014). Improved parameterization of seagrass blade dynamics and wave attenuation based on numerical and laboratory experiments. *Limnology and Oceanography*, 59(1):251 – 266.

Zeller, R. B., Zarama, F. J., Weitzman, J. S., and Koseff, J. R. (2015). A simple and practical model for combined wave-current canopy flows. *Journal of Fluid Mechanics*, 767:842 – 880, doi:10.1017/jfm.2015.59.

Zhang, X., Chua, V. P., and Cheong, H.-F. (2015). Geometrical and material properties of Sonneratia alba mangrove roots. *Trees*, 29:285 – 297.